

Section 1

Assimilation of atmospheric and land
observations.

Data impact and sensitivity studies.

Methodological advances.

A BACKGROUND ERROR COVARIANCE MATRIX FOR THE CPTEC DATA ASSIMILATION SYSTEM

Carlos Frederico Bastarz¹, Luiz Fernando Sapucci¹, João Gerd Zell de Mattos¹

¹Center for Weather Forecasts and Climate Studies, National Institute for Space Research, Cachoeira Paulista, São Paulo, Brasil
e-mail: carlos.bastarz@inpe.br

1. Introduction

The background error covariance matrix is one of the main components of a data assimilation system. At CPTEC, the past operational data assimilation system ran using available background error covariance matrices that used background information from other models/systems. CPTEC started to use the GSI as its operational data assimilation system, a GFS based background error covariance matrix was used as a starting point. Currently, CPTEC is preparing a new version of its global data assimilation system and a new background error covariance matrix was constructed using the NMC method and the pairs of forecasts of its global circulation model, the Brazilian Atmospheric Model (BAM, Figueroa et al., 2016). In this present work, we show the results of its application in a 3DVar data assimilation system by means of single observation assimilation experiment.

2. CPTEC New Background Error Covariance Matrix

The application of a new background error covariance matrix for a 3DVar global data assimilation system is shown here at a low resolution (TQ0062L028, roughly 200 km near the Equator with 28 sigma levels). This version was also applied to test a hybrid 3DVar system (CPTEC has plans to make it a future update to its global data assimilation). This matrix was calculated using the NMC method from a database of 1,460 pairs of 48 and 24 hours forecasts.

3. Single Observation Test Application within GSI and Future Plans

In order to test the new background error covariance matrix, we made a series of single observation tests. The single observation test is run under the GSI framework using a pure 3DVar system and makes use of a synthetic observation. With this type of tests, it is possible to control the magnitude of the observation error and innovation. Figure 1 shows the result of a single observation assimilation of zonal wind component placed at 250hPa, and centered at the point with coordinates 45°N, 180°W (lat x lon, respectively). Both the observation error and innovation magnitude were adjusted to 1 ms⁻¹. As the GSI allows for the application of the error covariances using an anisotropic filter, we also tested the application of the new background error covariance matrix using the anisotropic filter and compared its result against the GSI default matrix (using the same configuration) in order to see how the covariances accommodate the analysis increment. As can be seen, with the BAM/CPTEC background error covariance matrix, the resulting zonal wind analysis increment is broader than its GFS/NCEP counterpart. This may be due to a more detailed covariance structures (not shown) due to the use of a high number of forecast pairs. On the other hand, the application of the new BAM-based background error matrix should be properly tuned within GSI.

A complete version of this development was recently published in the Brazilian Journal of Meteorology, in which a more complete characterization of the new background error covariance matrix is made, accounting for its spatial features and quantitative characteristics.

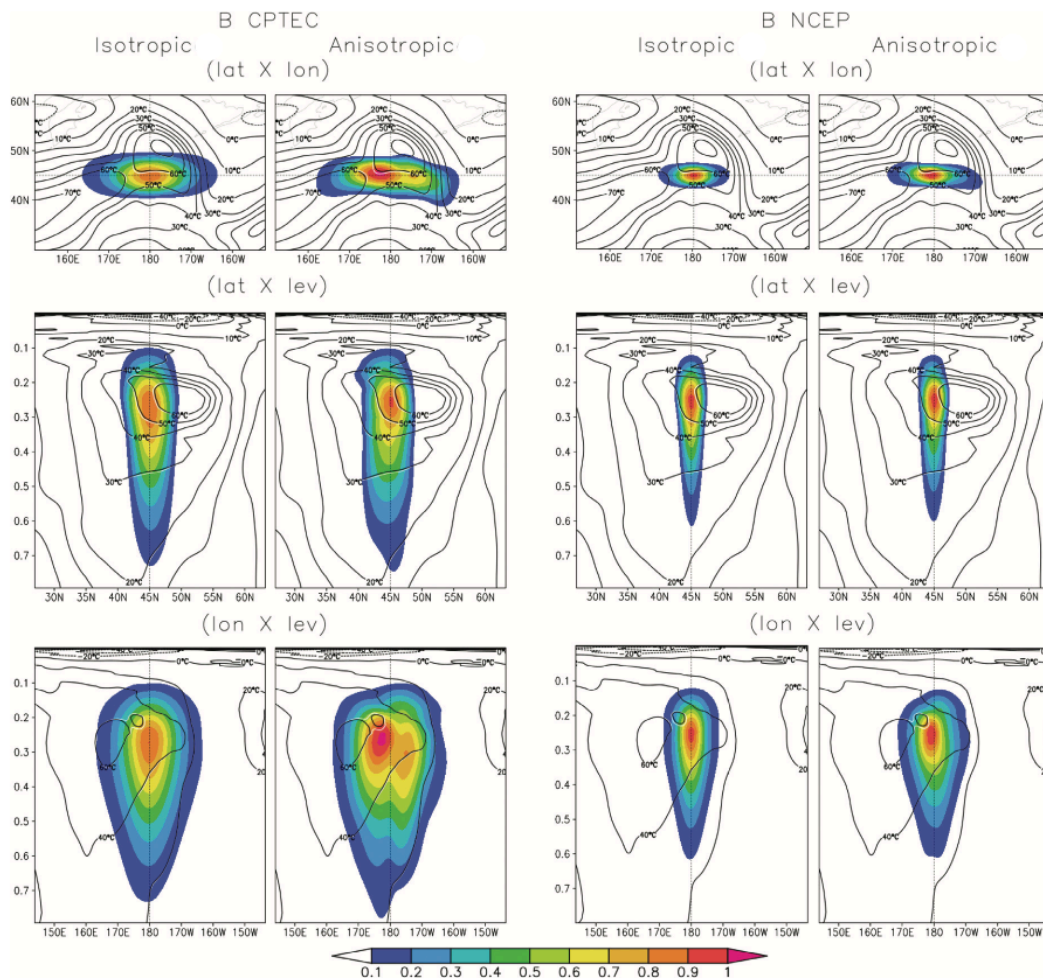


Figure 1. Horizontal wind (isolines) analysis increments (shaded) at 250 hPa, using the background error covariances matrices from CPTEC and NCEP, respectively. In the first row are shown the latitudinal sections, in the second rows, the longitudinal sections and in the third row, the vertical sections. At left, the analysis increment in isotropic and at right, the analysis increment is anisotropic.

References

Bastarz, C.F., D.L. Herdies, L.F. Sapucci, 2017: **Matriz de Covariâncias dos Erros de Previsão Aplicada ao Sistema de Assimilação de Dados Global do CPTEC: Experimentos com Observação Única. Background Error Covariance Matrix Applied to the Global Data Assimilation System at CPTEC: Single Observation Experiments.** Rev. bras. meteorol., São Paulo, v. 32, n. 3, p. 459-472, in Portuguese. Available from http://www.scielo.br/scielo.php?script=sci_arttext&pid=S0102-77862017000300459&lng=en&nrm=iso

Figuroa, S.N., J.P. Bonatti, P.Y. Kubota, G.A. Grell, H. Morrison, S.R. Barros, J.P. Fernandez, E. Ramirez, L. Siqueira, G. Luzia, J. Silva, J.R. Silva, J. Pendharkar, V.B. Capistrano, D.S. Alvim, D.P. Enoré, F.L. Diniz, P. Satyamurti, I.F. Cavalcanti, P. Nobre, H.M. Barbosa, C.L. Mendes, and J. Panetta, 2016: **The Brazilian Global Atmospheric Model (BAM): Performance for Tropical Rainfall Forecasting and Sensitivity to Convective Scheme and Horizontal Resolution.** Wea. Forecasting, 31, 1547–1572, <https://doi.org/10.1175/WAF-D-16-0062.1>

GSI-BASED HYBRID 3DVAR DATA ASSIMILATION FOR THE BAM-CPTEC/INPE

Carlos Frederico Bastarz¹, Dirceu Luis Herdies¹ and Luiz Fernando Sapucci¹

¹Center for Weather Forecasts and Climate Studies, National Institute for Space Research, Cachoeira Paulista, São Paulo, Brasil
e-mail: carlos.bastarz@inpe.br

1. Introduction

Recent developments in atmospheric data assimilation have demonstrated that hybrid methods are advantageous in allowing the introduction of background flow dependency into the specification of error correlations. This is one of the most challenging features to attain in an operational data assimilation system. At the beginning of its operations, CPTEC has experienced with its global circulation model the Optimum Interpolation technique, the Physical-space Statistical Analysis System (PSAS) and recently, the Gridpoint Statistical Interpolation (GSI) with the CPTEC Brazilian Atmospheric Model (BAM). The application of PSAS and GSI at CPTEC is the result of long-term collaboration between the CPTEC and the Global Modeling and Assimilation Office (GMAO/NASA). At the beginning of its operational use at the center, the GSI/3DVar were run using a static background error covariance matrix. This undergoing work reports some initial results with the application of a hybrid 3DVar data assimilation system using a linear combination of a static background error covariance matrix with an Ensemble Kalman (EnKF) filter based one.

2. A Global Hybrid 3DVar System for CPTEC

The CPTEC global hybrid 3DVar system is based on coupling between the GSI system (which provides the data assimilation framework including the traditional 3DVar method, an EnKF system and the framework through which the hybrid covariances are drawn) and the Brazilian Atmospheric Model (BAM, Figueroa et al., 2016). The observations assimilated within the system come from the Global Telecommunication System (GTS), which includes surface and upper-air observations, atmospheric retrievals and radiance observations from multiple satellites and sensors. The static part of the hybrid 3DVar background error covariance is modeled with the National Meteorological Center (NMC) method using pairs of 24-hour and 48-hour forecasts from the BAM model. In experimental mode, a database of 1,460 forecast pairs has been used to calculate the background error covariance matrix in a TQ0062L028 model resolution (roughly 200 km near the Equator with 28 sigma levels). The data assimilation cycle using the hybrid system applies the hybrid background error covariance matrix during the 3DVar minimization procedure (using the same methodology as described in Wang et al., 2013).

3. Resulting Hybrid Analysis and Future Plans

The hybrid 3DVar analysis cycle was tested using 50% and 75% of ensemble (40 members) contribution to the static part of the background error covariance matrix. The experiments included a control run with the NCEP analysis (no data assimilation), another control run with a pure 3DVar analysis and two runs using the hybrid analysis (with 50% and 75% of ensemble contribution). As a result, it was found that the hybrid (deterministic) analysis allowed the BAM model to perform better when 75% of ensemble contribution were used to determine the background error covariance (experiment EnSRF75). In terms of model skill, in general, the BAM model performed better with improvements in its prediction ability. Figure 1 shows the Anomaly Correlation for specific moisture at 925 hPa and zonal wind at 850 hPa for the South America region and for the whole Globe. As can be seen, the application of the hybrid method has a great advantage over the current and pure 3DVar in use at the center. Within the steep topography of the Andes

Mountains in South America, the forecast of moist processes, especially rain, is difficult. Improving the forecast of these processes can be also beneficial for the precipitation forecasts of the BAM model. Also, improving the wind forecasts (e.g., Figure 1c) is also beneficial because of the moisture transport by the Low-Level Jet to the southeast region of the continent. Further steps with the hybrid analysis should include tests with high resolution in order to properly access the precipitation forecasts.

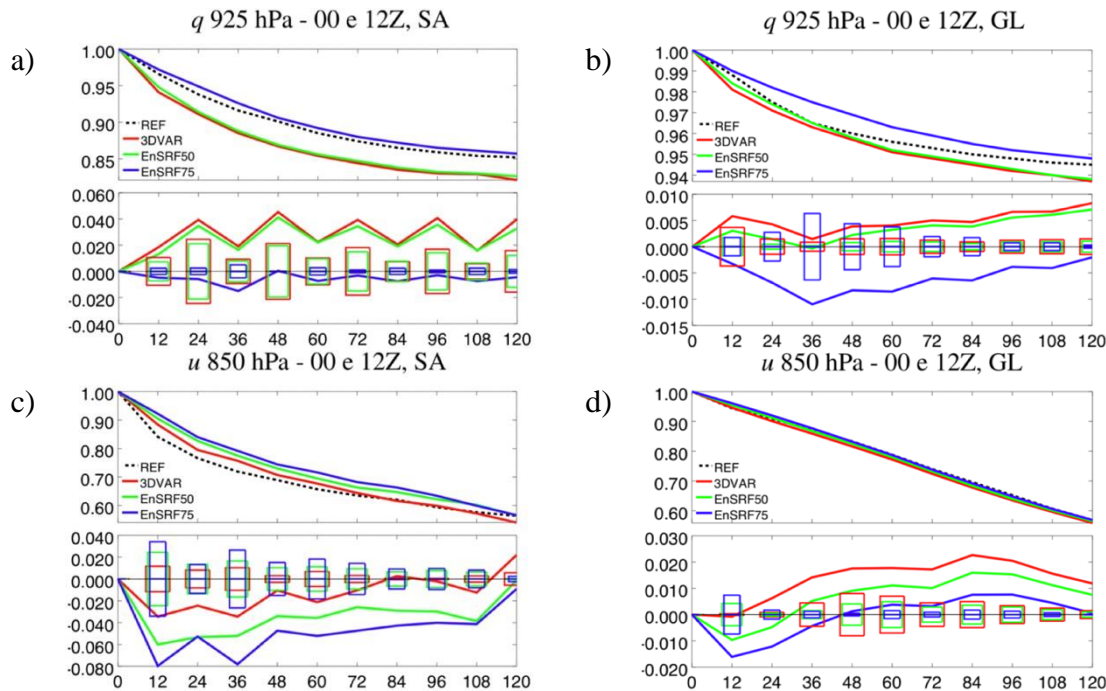


Figure 1. 5-day forecast skill for evaluated regions GL (global) and SA (South America). Dashed black lines: REF experiment (using the NCEP analyses); solid red line: pure 3DVar experiment; green line: EnSRF50 (using the 50% of the ensemble) and blue line: EnSRF75 (using 75% of ensemble). All figures are presented with their respective Student's t-test, where a 95% confidence interval is held.

CPTEC has also a global Ensemble Prediction System (EPS) which provides the center with extended range forecasts (up to 15 days). Currently, this system uses a perturbation approach based on an Empirical Orthogonal Functions methodology in order to provide the optimum perturbations to generate the ensemble members. As the tested hybrid 3DVar system makes use of an EnKF to both update the background ensemble members and to control the ensemble spread, a study is being made to access the ability of this system to provide an ensemble of analyses to serve as an upgrade to the current EPS system. Preliminary results show that at this lower analysis/model resolution, a proper configuration of the model should be defined to take in advantage the characteristics of the new system.

References

Figueroa, S.N., J.P. Bonatti, P.Y. Kubota, G.A. Grell, H. Morrison, S.R. Barros, J.P. Fernandez, E. Ramirez, L. Siqueira, G. Luzia, J. Silva, J.R. Silva, J. Pendharkar, V.B. Capistrano, D.S. Alvim, D.P. Enoré, F.L. Diniz, P. Satyamurti, I.F. Cavalcanti, P. Nobre, H.M. Barbosa, C.L. Mendes, and J. Panetta, 2016: **The Brazilian Global Atmospheric Model (BAM): Performance for Tropical Rainfall Forecasting and Sensitivity to Convective Scheme and Horizontal Resolution.** *Wea. Forecasting*, 31, 1547–1572.

Wang, X., D.F. Parrish, D. Kleist, and J. Whitaker, 2013: **GSI 3DVar-Based Ensemble-Variational Hybrid Data Assimilation for NCEP Global Forecast System: Single-Resolution Experiments.** *Monthly Weather Review*, 141 (11), 4098–4117.

Cycling Proactive Quality Control in GFS model

Tse-Chun Chen^{1,*} and Eugenia Kalnay¹

¹University of Maryland, College Park, MD, USA

*tcchen@umd.edu

Introduction

A fully flow-dependent Proactive Quality Control (PQC; [Ota et al., 2013](#); [Hotta et al., 2017](#)) that rejects detrimental observations identified by ensemble forecast sensitivity to observation (EFSO; [Kalnay et al., 2012](#)) was proposed to resolve the forecast skill dropout issues ([Kumar et al., 2017](#)). Successful and encouraging results obtained from non-cycling experiments using Global Forecasting System (GFS) from the National Centers for Environmental Prediction (NCEP), that denying the detrimental observations identified by EFSO with 24-hr and 6-hr verification lead-time both reduced forecast errors in several forecast skill dropout cases. In this study, we begin the examination of cycling PQC using the same complex GFS model.

Method and Experimental Setup

PQC corrects the analysis based on the observational impact from EFSO. Suppose the desired PQC time is $t = 0$ in a DA system with 6-hour assimilation window, the procedures are as follows:

1. Run standard DA cycle from $t = -6$ to $t = 6$ to get the analysis at $t = 6$ for verification.
2. Obtain 12-hour and 6-hour forecasts from $t = -6$ and $t = 0$.
3. Perform 6-hour EFSO with the above information to determine which observations should be rejected at $t = 0$.
4. PQC update the analysis without the rejected observations.

In this study, we utilize the GFS-LETKF system developed by [Lien \(2014\)](#) to test cycling PQC in the complex and realistic model. The resolution of GFS is T62 in order to save disk space and computational time. The assimilated observations are the prepBUFR data provided by NCEP. The experimental period spans from Jan/01/2008 to Feb/06/2008 and the first 5 days are discarded as DA spin-up period. In addition, the LETKF DA scheme with ensemble size of 32 instead of the GSI Hybrid EnVar used in operation is chosen for simplifying the procedure and expedition of the experiments since PQC should have little or no dependence on the DA methods. We chose 6 hours as the forecast error verification lead-time for EFSO impact evaluation and reject approximately 10 % of the overall most detrimental observations.

Results

We show the monthly mean of the GFS forecast relative improvement (%) by cycling PQC in [Figure 1](#). It is clear that for all regions and for the three listed key variables, the short-term forecast can be improved by as much as 10 % or more for higher latitudes. Then the improvement decreases with forecast time but saturates at around 5 % (not 0 %) even after 5 days.

The cycling PQC improvement is further broken down to direct impact (non-cycling PQC) and indirect (accumulated) impact (original analysis before PQC in cycling PQC experiment). As mentioned earlier, the direct impact comes from the PQC update from the original analysis at each cycle, which is equivalent to the non-cycling PQC. The main benefit of cycling PQC is the accumulation of the direct improvements throughout the past cycles that the improved forecast initiated from the PQC corrected analysis serves as a much accurate background and further boost the accuracy of the following analyses. We separate the indirect impact from the full impact by verifying the forecasts initiated not from the PQC corrected analysis but the original analysis before PQC. As we can see, the major advantage of cycling PQC is from the accumulation of past direct improvements and the independent direct improvement is only 2 % at most. It is also noticeable that the benefit from the direct impact has a larger contribution to the full impact in the tropics and the southern hemisphere comparing to that in the northern hemisphere. This indicates that the PQC improvement in the northern hemisphere has a shorter memory on average.

Discussion

The fact that the accumulation of past impact contributes to a major portion of the full impact of cycling PQC has two important implications. One is that the PQC improvement has a long-term memory and remains in the system even after several cycles of DA. Secondly, this supports the feasibility of implementing PQC in operational NWP. In order to deliver the forecast products on time, the operational centers need to initiate the forecast as soon as the analysis is completed, so we can only afford to

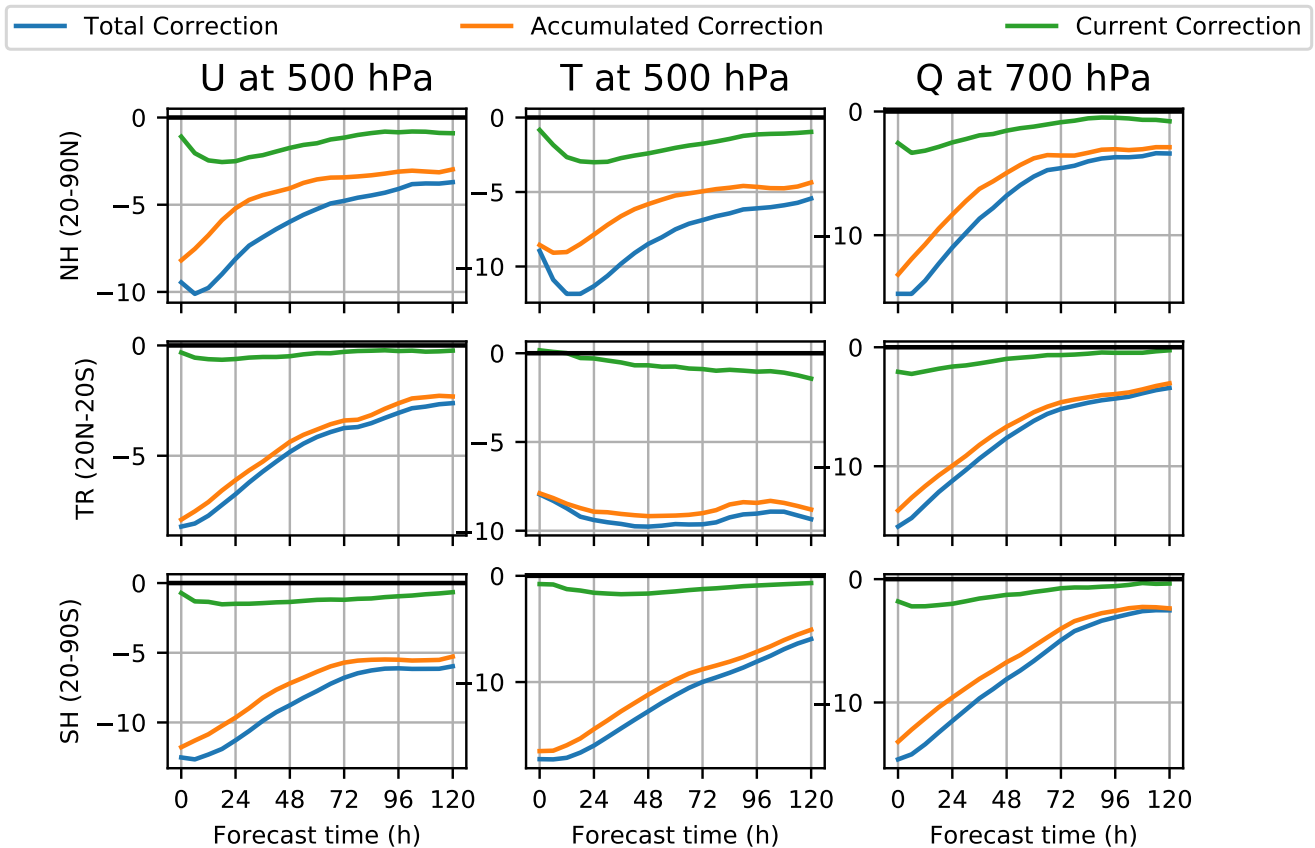


Figure 1. Monthly mean relative forecast error (RMSE) reduction percentage initiated from cycling PQC analysis, original analysis in cycling PQC experiment, and non-cycling PQC in u-component wind at 500 hPa, temperature at 500 hPa, and specific humidity at 700 hPa for the northern hemisphere (20N-90N), the tropics(20N-20S), and the southern hemisphere(20S-90S) throughout 5 days.

perform PQC after the current forecast is out, meaning the direct impact from PQC is not available in operation. Therefore, the huge portion of accumulated indirect impact sends a very encouraging message that even without the direct impact of the current observations we can still get a forecast improvement close to the full impact.

References

- Hotta, D., T.-C. Chen, E. Kalnay, Y. Ota, and T. Miyoshi, 2017: Proactive QC: A Fully Flow-Dependent Quality Control Scheme Based on EFSO. *Monthly Weather Review*, **145** (8), 3331–3354, doi:10.1175/MWR-D-16-0290.1, URL <http://journals.ametsoc.org/doi/10.1175/MWR-D-16-0290.1>.
- Kalnay, E., Y. Ota, T. Miyoshi, and J. Liu, 2012: A simpler formulation of forecast sensitivity to observations: application to ensemble Kalman filters. *Tellus A*, **64**, 1–9, doi:10.3402/tellusa.v64i0.18462, URL <http://www.tellusa.net/index.php/tellusa/article/view/18462/xml><http://www.tellusa.net/index.php/tellusa/article/view/18462>.
- Kumar, V. K., A. Eichmann, J. Alpert, and S. Boukabara, 2017: Global Forecast Dropout Prediction Tool in Support of the NCEP Model Evaluation Group (MEG)—Collaboration Project Between JCSDA/NESDIS & NWS. *JCSDA Quarterly*, (55), 5–13, doi:10.7289/V5V98648.
- Lien, G.-y., 2014: Assimilation of Satellite Precipitation Analysis with the GFS-LETKF System. Ph.D. thesis, Ph. D. Prospectus, University of Maryland.
- Ota, Y., J. C. Derber, E. Kalnay, and T. Miyoshi, 2013: Ensemble-based observation impact estimates using the NCEP GFS. *Tellus A*, **65**, 20 038, doi:10.3402/tellusa.v65i0.20038, URL <http://www.tellusa.net/index.php/tellusa/article/view/20038/xml>.

Proactive Quality Control in Lorenz (1996) model

Tse-Chun Chen^{1,*} and Eugenia Kalnay¹

¹University of Maryland, College Park, MD, USA

*tcchen@umd.edu

Introduction

Proactive Quality Control (PQC; Ota et al., 2013; Hotta et al., 2017) based on EFSO was proposed aiming to resolve the forecast skill dropout issues (Kumar et al., 2017) through identification and rejection of detrimental observations that may be harmful to the forecast. They showed using the Global Forecasting System (GFS) from the National Centers for Environmental Prediction (NCEP), that denying the detrimental observations identified by ensemble forecast sensitivity to observation (EFSO Kalnay et al., 2012) with 24-hr and 6-hr verification lead-time both reduced forecast errors in several forecast skill dropout cases. Hence, it was further proposed that PQC would be affordable in operational cycling to reduce or avoid skill dropouts in an online fashion. A major potential benefit in cycling-PQC is that the improved forecast may serve as a better background and lead to a cumulative improvement in the following analyses and forecasts. However, cycling-PQC has not been thoroughly tested yet. Idealized simulation experiments in a controlled environment can provide insights on how to optimally set up cycling PQC for realistic models.

Methods

The essential concept of PQC is to utilize the EFSO impact as observational QC for each DA cycle (e.g., 6 hours) for the identification of detrimental observations. The analysis is then modified to avoid the impact of those identified detrimental observations. It should be noted that EFSO cannot be computed until the next analysis becomes available for forecast error verification. The PQC algorithm can be summarized as inserting additional steps (verifying analysis for EFSO, EFSO computation, PQC analysis update, and the forecast from the updated analysis) into a standard DA cycle. The focus of this study is to compare the performance of five possible PQC analysis updates defined in Table 1.

Table 1. PQC update methods

Methods	Mechanism	Change in \mathbf{K}	Change in Spread	Repeat analysis	Computational cost
PQC_H	Recompute \mathbf{K} without rejected observations	Large	Increased	Yes	High
PQC_R	Recompute \mathbf{K} with up-weighted \mathbf{R}	Large	Increased	Yes	High
PQC_K	Reuse the original EFSO \mathbf{K}	None	None	No	Low
PQC_BmO	Assimilate background minus observation	Low	Reduced	(Serial update)	Medium
PQC_AmO	Assimilate analysis minus observation	Low	Reduced	(Serial update)	Medium

Results

Figure 1 compares the performance of all proposed PQC methods using EFSO (verified at 6-steps) and with varying percentages of rejected observations. Since the Kalman gain \mathbf{K} of PQC_R approaches that of PQC_H asymptotically with increasing observational error, it is not surprising that PQC_H and PQC_R methods perform more or less the same in terms of both analysis and 30-step forecast error reduction. The errors are reduced the most when rejecting 10 % of the observations for the two methods. It is somewhat surprising that PQC_K, PQC_BmO, and PQC_AmO all outperform PQC_H and PQC_R, which are two most commonly used data denial methods. For the analysis quality improvement, the obvious choice of the threshold shifts towards 20%. PQC_K does not show any degradation of analysis until rejecting more than 60 % of the observations, whereas PQC_BmO and PQC_AmO stop showing improvement after 50% and even suffer from filter divergence beyond 60%. For the forecast quality improvement, the dependence of PQC_BmO and PQC_AmO on the thresholds are qualitatively similar to that in analysis performance. It is quite shocking to find that PQC_K has nearly no dependence on the thresholds between 10-th and 60-th percentile, especially when compared to the 10% optimal choice for PQC_H and PQC_R.

Discussion

Intuitively, the “flat bottom” of PQC_K (rather than the “check mark” shape of PQC_H and PQC_R) is more consistent with the estimated impact of the observations since the magnitude of the impacts between 10-th to 60-th percentile is really

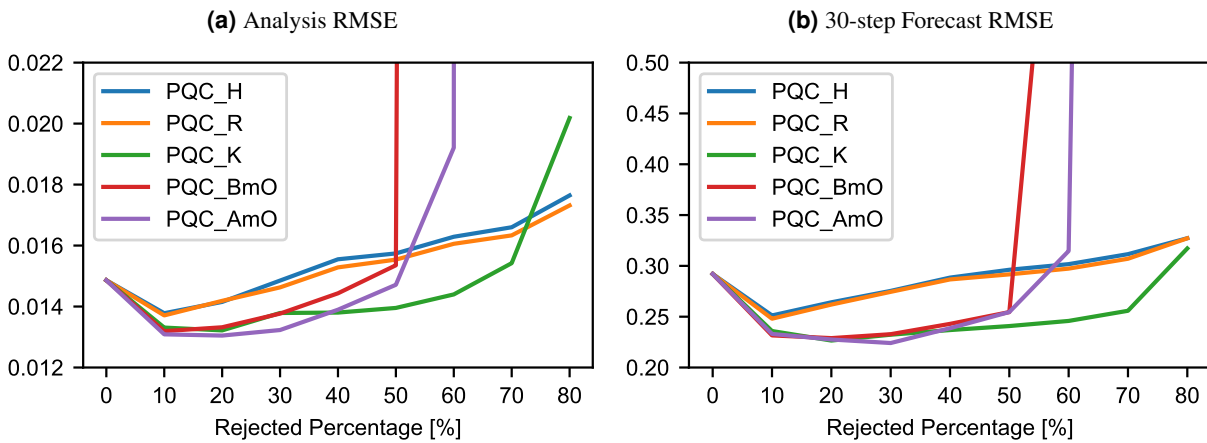


Figure 1. Performance of 6-step PQC with all 5 methods in terms of (a) analysis RMSE and (b) 30-step forecast RMSE as a function of rejection percentage.

small compared to that of those below 10-th percentile. And hence it should be insensitive (“flat bottom”) to rejecting those observations between 10-th to 60-th percentile. This explains why the results are better for PQC_K than for PQC_H since PQC_K is more consistent with the nature of the computation of EFSO and the estimated impact. Note that EFSO provides the estimated impacts of each observation in the presence of all other assimilated observations, and hence the impacts remain valid as long as \mathbf{K} does not change much. However, PQC_H and PQC_R significantly change \mathbf{K} when rejecting some observations, thereby the accuracy of the estimated EFSO impacts becomes lower, and the PQC based on those impacts does not work as desired. The total AIs obtained at the end of the update consists of the AIs contributed from each individual observation and it is the AIs that determines the forecast error changes rather than the observation innovation. Hence, PQC should target the AIs corresponding to the detrimental observations rather than the observations themselves. And simple data denial by manipulating \mathbf{H} and \mathbf{R} does not necessarily reject the AIs that lead to forecast degradation especially when rejecting an excessive number of observations. PQC_K, by contrast, uses the exact same \mathbf{K} to reject the exact detrimental AIs identified by EFSO and ends up with even larger improvements. In addition, the observations with largest impacts contribute to AIs among the most unstable modes, while the less impactful observations are associated with the neutral and stable modes which have little or no error growth. Hence, after rejecting the few very detrimental AIs, it does not matter much whether those less impactful AIs are rejected since the difference is very unlikely to grow in the future, thereby showing the “flat bottom” feature in the center of Fig. 1.

For PQC_BmO and PQC_AmO, they change \mathbf{K} in a less radical fashion by “assimilating” new observations to the original analysis and yield improvements similar to PQC_K with a small number of rejected observations. But they suffer from filter divergence easily with a large number of rejected observations since the ensemble becomes overly confident due to the “additional” assimilation of opposite innovations. It is worth noting that the commonly observed difference in the impact estimated by EFSO and observing system experiments/ data denial experiments corresponds to the difference in PQC_K and PQC_H.

References

- Hotta, D., T.-C. Chen, E. Kalnay, Y. Ota, and T. Miyoshi, 2017: Proactive QC: A Fully Flow-Dependent Quality Control Scheme Based on EFSO. *Monthly Weather Review*, **145** (8), 3331–3354, doi:10.1175/MWR-D-16-0290.1, URL <http://journals.ametsoc.org/doi/10.1175/MWR-D-16-0290.1>.
- Kalnay, E., Y. Ota, T. Miyoshi, and J. Liu, 2012: A simpler formulation of forecast sensitivity to observations: application to ensemble Kalman filters. *Tellus A*, **64**, 1–9, doi:10.3402/tellusa.v64i0.18462, URL <http://www.tellusa.net/index.php/tellusa/article/view/18462/xmlhttp://www.tellusa.net/index.php/tellusa/article/view/18462>.
- Kumar, V. K., A. Eichmann, J. Alpert, and S. Boukabara, 2017: Global Forecast Dropout Prediction Tool in Support of the NCEP Model Evaluation Group (MEG)—Collaboration Project Between JCSDA/NESDIS & NWS. *JCSDA Quarterly*, (55), 5–13, doi:10.7289/V5V98648.
- Ota, Y., J. C. Derber, E. Kalnay, and T. Miyoshi, 2013: Ensemble-based observation impact estimates using the NCEP GFS. *Tellus A*, **65**, 20038, doi:10.3402/tellusa.v65i0.20038, URL <http://www.tellusa.net/index.php/tellusa/article/view/20038/xml>.

Land Data Assimilation at CPTEC/INPE Atmospheric Global Circulation Model

JOÃO G. Z. DE MATTOS*, ARIANE FRASSONI, LUIS G. G. DE GONÇALVES, DIRCEU L. HERDIES

Center for Weather Forecasting and Climate Studies, National Institute for Space Research

1. Introduction

During the last decade, an ever growing number of numerical sensibility studies suggested that atmospheric variability is strongly influenced by the land-atmosphere coupling, in particular due to soil moisture anomalies. Indeed, soil moisture impacts the atmosphere by controlling the evaporation component in the surface water and energy balance equations. Through variations in the evaporation, soil moisture also affects the sensible (H) and latent heat fluxes (E). Therefore, soil moisture is capable of producing changes in the atmospheric temperature and humidity and can also impact precipitation (Seneviratne et al. 2010). On the one hand, there is a control in the amount of evaporation and consequently, water availability in the atmosphere for precipitation.

Soil moisture also impacts the Planetary Boundary Layer (PBL) through H and E , changing temperature and humidity and affecting its vertical development. This is crucial for convective triggering (Gentine et al. 2013), especially over Amazon Basin, where precipitation has a diurnal cycle marked by the occurrence of precipitation peaks hours after the maximum solar radiation. Bechtold et al. (2004) and Santos e Silva et al. (2012) using numerical simulations showed that the improvement in the representation of the diurnal cycle of precipitation over tropical region of South America is related with better representation of convective trigger when the convective parameterization is coupled to H and E .

By the importance of soil moisture for numerical weather and climate prediction, especially for the precipitation forecasts, we have applied a soil moisture data assimilation technique developed by (Mahfouf 1991) to better represent the soil moisture states in the initial conditions of the Brazilian global Atmospheric circulation Model (BAM) of the Center for Weather Forecasting and Climate Studies of the Brazilian National Institute for Space Research (CPTEC/INPE). In the next section we present a

short description of the data assimilation technique and a general description of the numerical experiment performed.

2. Methodology and experimental design

a. Surface analyses

In the method proposed by Mahfouf (1991), near surface meteorological observations measured routinely and transmitted throughout the Global Telecommunication System (GTS) can be used to estimate soil moisture. In this method, an independent two-dimensional statistical interpolation is performed to analyze 2-m temperature and relative humidity. The analysis increment for these two variables are used to analyze the water content of all soil layers of BAM land surface model. Each soil layer is analyzed separately; however, in the following equations subscripts indicating the soil layer are omitted:

$$\delta\theta = \alpha \times (T_a - T_b) + \beta \times (rH_a - rH_b), \quad (1)$$

where T_a and T_b are the analyzed and background 2-m temperature and rH_a and rH_b are the analyzed and background 2-m relative humidity. The analysis relies essentially on the coefficients and, also known as optimum coefficients, which are computed following Douville et al. (2000).

b. Numerical experiment

Two long-range runs of 17 years were performed to verify if better representation of the soil moisture states in the initial conditions of the BAM can improve the precipitation simulations. Both simulations were initialized from the same atmospheric initial conditions and forced by the same Sea Surface Temperature (SST). The first experiment is a Open Loop (OL) in which the soil moisture evolves freely. Another experiment considers the method proposed by Mahfouf (1991) (Land Data Assimilation [LDAS]), with a data assimilation cycle of 6 hours with soil moisture correction by increments of atmospheric 2-m temperature and humidity.

* *Corresponding author address:* João G. Z. de Mattos, Center for Weather Forecasting and Climate Studies, Rodovia Presidente Dutra Km 40, Cachoeira Paulista, SP, Brazil
E-mail: joao.gerd@inpe.br

3. Results

Differences between the simulations with and without soil moisture data assimilation indicate that in general, occurs a constant addition of water in the soil, suggesting the presence of systematic errors in the model, especially in North and South American continents (figure not shown). These errors can be associated with simplifications and deficiencies in the land surface model instead random errors from the atmospheric forcing. Nevertheless, consecutive changes in the soil water content (positive or negative increment of soil moisture) impact horizontal distribution of soil moisture and consequently E and H fluxes.

The cumulative effect of the changes improves the amount of soil moisture in some regions leading to an improvement in the forecast of the variables in lower troposphere, mainly the relative humidity (not shown). These modifications contributed to a better representation of the mean annual precipitation cycle over different regions of the world. In the Figure 1 it is presented the global mean annual cycle of precipitation. The correlation between each experiment and Climate Prediction Center – Merged Analysis of Precipitation (Xie and Arkin 1997, CMAP) data is 0.4 in OL and 0.8 in LDAS experiment. Major improvement has occurred from July to October.

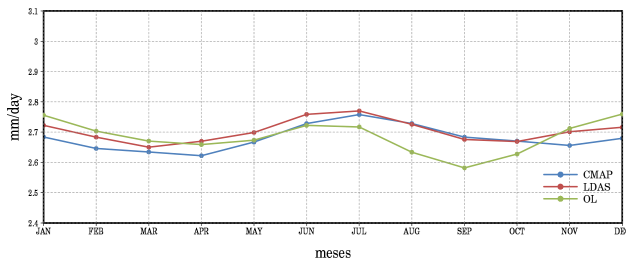


FIG. 1. Global mean annual cycle of precipitation (mm/day). Green line represents the OL experiment, red line the soil moisture data assimilation run and blue line represents CMAP observational data.

Figure 2 shows the annual mean difference between monthly total precipitation from LDAS and OL experiments. Improvements are noticed over North and South American continents, in particular over Amazon Basin and Southern South America.

The regions of higher improvements are similar to spatial patterns showed by Global Land–Atmosphere Coupling Experiment (Koster et al. 2006, GLACE) reinforcing the coupling strength over these regions.

4. Concluding remarks

The use of soil moisture data assimilation contributed to a better representation of the mean annual cycle of precipitation over different regions of

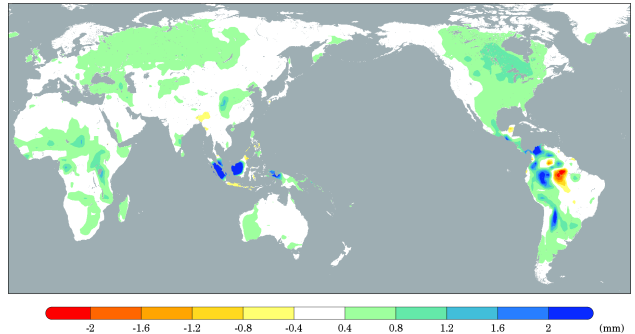


FIG. 2. Annual mean of the difference between monthly total precipitation produced by the LDAS and OL experiments.

the world, like North and South American continents, Africa and Northern Europe. Differences between total precipitation showed some improvement of precipitation over regions similar to the spatial patterns showed by GLACE, reinforcing the coupling strength of soil moisture and precipitation over some regions of world.

Due to improvement in the annual cycle of precipitation in this long-range run, the present study shows a potential benefits in the use of a soil moisture data assimilation to improve BAM for seasonal forecasting applications. Such investigation will be explored in future studies.

References

- Bechtold, P., J. P. Chaboureau, A. Beljaars, A. K. Betts, M. Köhler, M. Miller, and J. Redelsperger, 2004: The simulation of the diurnal cycle of convection precipitations over land in a global model. *Quarterly Journal Royal Meteorological Society*, **130** (604), 3119–3137.
- Douville, H., P. Viterbo, J.-F. Mahfouf, and A. C. M. Beljaars, 2000: Evaluation of the optimum interpolation and nudging techniques for soil moisture analysis using FIFE data. *Monthly Weather Review*, **128** (6), 1733–1756, URL [http://dx.doi.org/10.1175/1520-0493\(2000\)128<1733:EOTOIA>2.0.CO;2](http://dx.doi.org/10.1175/1520-0493(2000)128<1733:EOTOIA>2.0.CO;2).
- Gentine, P., A. a. M. Holtslag, F. D’Andrea, and M. Ek, 2013: Surface and atmospheric controls on the onset of moist convection over land. *Journal of Hydrometeorology*, **14** (5), 1443–1462, doi:10.1175/JHM-D-12-0137.1.
- Koster, R. D., and Coauthors, 2006: GLACE: The global land–atmosphere coupling experiment. Part I: Overview. *Journal of Hydrometeorology*, **7** (4), 590–610.
- Mahfouf, J.-F. c., 1991: Analysis of soil moisture from near–surface parameters: A feasibility study. *Journal of Applied Meteorology*, **30** (11), 1534–1547.
- Santos e Silva, C. M., S. R. de Freitas, and R. Gielow, 2012: Numerical simulation of the diurnal cycle of rainfall in sw amazon basin during the 1999 rainy season: the role of convective trigger function. *Theoretical and Applied Climatology*, **109**, 473.
- Seneviratne, S. I., T. Corti, E. L. Davin, M. Hirschi, E. B. Jaeger, I. Lehner, B. Orlowsky, and A. J. Teuling, 2010: Investigating soil moisture–climate interactions in a changing climate: A review. *Earth-Science Reviews*, **99** (3–4), 125–161, doi:10.1016/j.earscirev.2010.02.004, URL <http://dx.doi.org/10.1016/j.earscirev.2010.02.004>.
- Xie, P., and P. a. Arkin, 1997: Global precipitation: A 17-year monthly analysis based on gauge observations, satellite estimates, and numerical model outputs. *Bulletin of the American Meteorological Society*, **78**, 2539–2558, doi:10.1175/1520-0477(1997)078<2539:GPAYMA>2.0.CO;2.

Evaluation and Correction of Observations in Atmospheric Channels of the Satellite Microwave Radiometer MTVZA-GY

Dmitry Gayfulin⁽¹⁾, Michael Tsyrunikov⁽¹⁾ ¹ and Alexander Uspensky⁽²⁾

⁽¹⁾ *HydroMetCenter of Russia*

⁽²⁾ *State Research Center “Planeta”, Russia*

Abstract

Data in atmospheric sounding channels of the microwave radiometer MTVZA-GY on board the Russian satellite Meteor-M N2 are examined. An adaptive correction technique for MTVZA-GY antenna temperatures is motivated and developed. The technique accounts for the solar angles and sequentially assimilates observed minus simulated radiances in a perpetual 24h cycle in order to estimate up-to-date correction coefficients defined to be functions of the zenith and azimuth solar angles. The accuracy of corrected MTVZA-GY observations is compared with the accuracy of AMSU-A and MHS data.

Description

MTVZA-GY is a 29-channel microwave imaging/sounding radiometer (with conical scan geometry) somewhat similar to SSMIS or AMSU-A and MHS combined. MTVZA-GY data are available to direct readout users. Importantly, MTVZA-GY is supported by the radiative transfer model RTTOV starting from its version 11. For more, see Gayfulin et al. (2018) and the WMO OSCAR web site.

The MTVZA-GY radiometer on board Meteor-M N2 is, unfortunately, currently not working properly (since 15 August 2017). The next MTVZA-GY instrument is planned to be launched by the end of 2018. In total, 4–5 satellites of the Meteor-M type with the MTVZA-GY sensor on board are to be launched till 2025 in both the morning and the afternoon orbits.

Motivation

1. Soon after launch large biases in antenna temperatures were found. These were mitigated by a the simple linear scheme, which can be viewed as a kind of recalibration: $T_b = aT_a + b$, where T_a is the antenna temperature, T_b is the recalibrated brightness temperature, and a and b are the regression coefficients (estimated from a training sample).

Recalibrated and bias-corrected MTVZA-GY data were assimilated by Gayfulin et al. (2017) in the meteorological data assimilation system of the HydroMetCentre of Russia. A significantly positive impact of MTVZA-GY observations in the Southern Hemisphere in the absence of AMSU-A observations was found. However, it was felt that further improvements in the data accuracy were possible.

2. It was found that after the “simple correction” $T_b = aT_a + b$, observation errors (evaluated against the background defined to be the 6h NCEP GFS forecast converted to radiances by the RTTOV model) were dependent on the *solar angles* (the zenith angle ζ and the azimuth angle α), see Fig.1 (upper panels). This led us to devise a correction scheme that exploits the solar angles dependencies in order to improve the data.

Solar-angles dependent correction (SAC) technique

To account for the dependence of the observation error on the solar angles, we let the two coefficients, a and b , of the above “simple correction” scheme be functions of the solar angles α and ζ :

$$T_b = a(\alpha, \zeta) \cdot T_a + b(\alpha, \zeta). \quad (1)$$

The gridded fields $a(\alpha, \zeta)$ and $b(\alpha, \zeta)$ required for the application of the correction model Eq.(1) are cyclically updated (i.e. sequentially estimated) every 24 hours in a variational scheme, which aims to minimize the cost function

$$J(\mathbf{a}, \mathbf{b}) = J_{\text{obs}}(\mathbf{a}, \mathbf{b}) + J_{\text{fg}}(\mathbf{a}, \mathbf{b}) + J_{\text{smo}}(\mathbf{a}, \mathbf{b}) \rightarrow \min, \quad (2)$$

where \mathbf{a} and \mathbf{b} are the vectors that represent the coefficient fields $a(\alpha, \zeta)$ and $b(\alpha, \zeta)$, J_{obs} penalizes deviations of observations (T_a) from the background, J_{fg} regularizes the problem and allows assimilation

¹Correspondence to michael.tsyrunikov@gmail.com

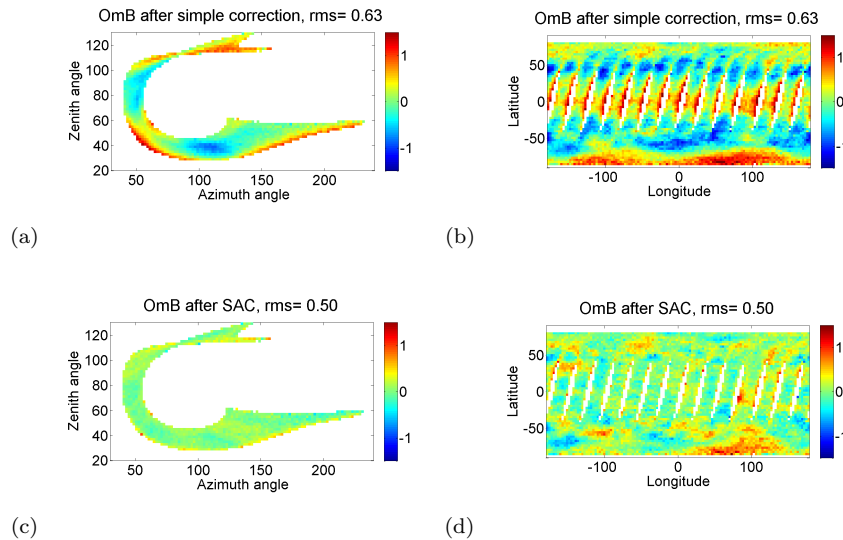


Figure 1: Local biases for observations in channel 18 valid at times from 21h UTC, 12 June 2017 to 3h UTC, 14 June 2017 (descending orbits). *Top*: After the “simple” correction (with constant coefficients a and b). *Bottom*: After SAC. *Left*: On the α - ζ plane. *Right*: On the geographic map

of past data by controlling deviations from a *first guess* (persistence forecast of \mathbf{a} and \mathbf{b} from the previous cycle), and J_{smo} further regularizes the problem by imposing a smoothness constraint on the fields \mathbf{a} and \mathbf{b} . See Gayfulin et al. (2018) for more details.

Evaluation results

Three two-week periods in summer, winter, and spring/fall were selected for numerical experiments. The application of the estimated SAC correction model to independent observations was shown to significantly improve their accuracy (as compared to the above “simple correction”, in which a and b are constants). The MTVZA-GY errors were compared with errors in the respective/similar channels of AMSU-A and MHS sensors for the same time periods. As compared with AMSU-A observations, corrected MTVZA-GY data in temperature sounding channels appeared to be 1–3 times less accurate. In atmospheric humidity sounding channels, the corrected MTVZA-GY observations are about 1.5–2 times less precise than the MHS data.

Local biases for SAC-corrected observations are presented in Fig.1 (lower panels). In this figure, comparing the lower panels (the SAC scheme) with the upper panels (the “simple” scheme) demonstrates how successfully the developed SAC scheme removes the local biases, leaving behind, largely, just noise.

Bibliography

- D. Gayfulin, M. Tsyruльников, A. Uspensky, E. Kramchaninova, S. Uspensky, P. Svirenko, and M. Gorbunov. The usage of MTVZA-GYa satellite microwave radiometer observations in the data assimilation system of the Hydrometcenter of Russia. *Russian Meteorology and Hydrology*, 42(9):564–573, 2017. doi: 10.3103/S1068373917090035.
- D. Gayfulin, M. Tsyruльников, and A. Uspensky. Assessment and adaptive correction of observations in atmospheric sounding channels of the satellite microwave radiometer MTVZA-GY. *Pure and Applied Geophysics*, v. 175, 2018. doi: 10.1007/s00024-018-1917-7. View-only link to the published article: <https://rdcu.be/YLSw>.

About inertia of measurement devices

Vladimir A. Gordin.

National Research University Higher School of Economics &
Hydrometeorological Center of Russia, Moscow, Russia. vagordin@mail.ru

A usual model for measuring device readings is based on the following differential relation:

$$d_t u = -k(u - f)|u - f|^b, k, b = \text{const}, k > 0. \quad (1)$$

Here $u(t)$ is the measuring device reading, and $f(t)$ is the true value of the measured parameter, t is the time, and k is the parameter characterizing the device inertia. The simplest version is: $b=0$.

We obtain some data $\{u_j\}_{j=1}^n$ as a result of aerological measurements at time moments $\{t_j\}_{j=1}^n$, and use a finite-difference scheme to approximate (1) and evaluate the true signal $f(t)$. A compact difference scheme (see e.g. [1]) provides high approximation order and can help us to avoid a significant amplification of high frequencies in the evaluation of $f(t)$.

The inertia parameter k is not constant and depends, e.g. on temperature, see [2]. We can evaluate it (e.g. for a humidity-measuring device) in laboratory experiments under constant temperature: $\lim_{t \rightarrow \infty} k(t) = K_\infty(T)$.

However, the inertia of a real device cannot change immediately with a change of temperature $T=T(t)$. It can be essential when variations of temperature T with height are strong (e.g. when the device is located on a radiosonde).

In this case we should modify model (1) and use the system

$$d_t u = -k(t) \cdot (u - f) \Rightarrow f = u + k^{-1}(t) \cdot d_t u,$$

$$d_t k = A \cdot [K_\infty(T(t)) - k] \Rightarrow k(t) = K_\infty(T(0)) + \int_0^t K_\infty(T(s)) e^{A(s-t)} ds,$$

where A is a constant. Compact finite-difference scheme are useful for approximation of the differential connections (see e.g. [1]).

We assume that the temperature $T(t)$ is known. Beforehand we evaluate the constant A in additional laboratory experiments.

We recommend to use the algorithm for BUFR data assimilation.

The article was prepared within the framework of the Academic Fund Program at the National Research University Higher School of Economics (HSE) in 2018 - 2019 (grant № 18-05-0011) and supported within the framework of a subsidy granted to the HSE by the Government of the Russian Federation for the implementation of the Global Competitiveness Program.

References

1. V.A.Gordin. Differential and Finite-Difference Equations. What Are Phenomena That They Described, And How They Are Solved. "Publisher House of Higher School of Economics", Moscow, 2016 (In Russian).

2. L.M.Miloshevich. Correction of Vaisala RS92 Radiosonde Humidity Measurements. 2011. http://milo-scientific.com/prof/corr_method.php

Ensemble-based Observation Impact Development at EMC

David Groff*¹, Kayo Ide³, Yanqiu Zhu¹, Rahul Mahajan¹, Daryl Kleist², Andrew Collard¹, John Derber²

¹I.M. Systems Group, College Park, Maryland

²NOAA/NWS/NCEP/Environmental Modeling Center, College Park, Maryland

³University of Maryland, College Park, Maryland

*Correspondence to: 5830 University Research Ct., College Park, MD 20740; email: david.groff@noaa.gov

The ensemble forecast sensitivity to observations (EFSO) formulation (Kalnay et al. 2012) has been implemented (Ota et al. 2013 and Groff et al. 2017) in the source code that provides ensemble square root filter (EnSRF) (Whitaker and Hamill 2002) functionality at the National Centers for Environmental Prediction (NCEP). As with the adjoint-based forecast sensitivity observation impact (FSOI) approach, the ensemble-based observation impact approach effectively enables a simultaneous computation of estimated forecast impacts and sensitivities for any and all observations assimilated in a numerical weather prediction (NWP) system. The NCEP GFS applies 4D ensemble-variational (4DEnVar) data assimilation (Kleist et al. 2015), and as such, requires an ensemble of short range forecasts to provide flow-dependent background uncertainty information. As currently configured, the EnSRF data assimilation algorithm is applied to assist in the assignment of initial conditions for the aforementioned ensemble of short range forecasts. In the context of 4DEnVar GFS cycling and following the EFSO approach described in Kalnay et al. 2012, the ensemble of analyses resulting from the EnSRF update have been used in representation of analysis-error covariance, and accordingly in approximation of the EnSRF Kalman gain. EFSO calculations are then based on the projection of this approximate Kalman gain to an evaluation forecast time using the gfs forecast model.

A complication with applying EFSO in the aforementioned context is that the set of observations and observation types assimilated in the GFS applied configuration of EnSRF are not representative of what is assimilated during the variational minimization (Todling and Diniz 2018). A variance-reduction based approach to discarding observations during the EnSRF update accounts for most of this discrepancy. To alleviate this impediment to achieving representative EFSO datasets for the aforementioned context, beta testing has been performed for GFS applied EnSRF configurations in which the variance-reduction based data discarding is disabled. Moving forward, modified pure ensemble sensitivity-based approaches will be explored to achieve a more robust observation impact approach.

In the EFSO approach, cross-covariances between perturbations in observation space and perturbations for a choice of metric in state space at the evaluation forecast time are employed to enable comparison of background states and individual observations at the evaluation forecast time. As such, taking advantage of the simultaneity aspect of EFSO datasets enables an objective basis for identifying where and when assimilated observation types are relatively more (less) efficient in reducing forecast error. Figures 1 and 2, see captions, show partitioning of 24 hour EFSO datasets (i.e. estimates for reduction of 24 hour forecast error) for the moist total

energy norm (Ehrendorfer et al. 1999) by location and innovation. Similarly, EFSO simultaneity can be applied as a basis for hyperspectral IR channel selection. 24 hour EFSO calculations for IASI, AIRS and CrIS (not shown) indicate that assimilated 11 μm surface channels and 9.6 μm ozone band channels are relatively inefficient in reducing forecast error for the moist total energy norm.

Although the EFSO methodology provides an objective basis for estimating observation forecast impacts, the extent to which the approach provides representative information for improving global forecast system (GFS) or global ensemble forecast system (GEFS) forecast skill has yet to be rigorously tested. As such, it is planned that several EFSO guided experiments will be performed in the next year.

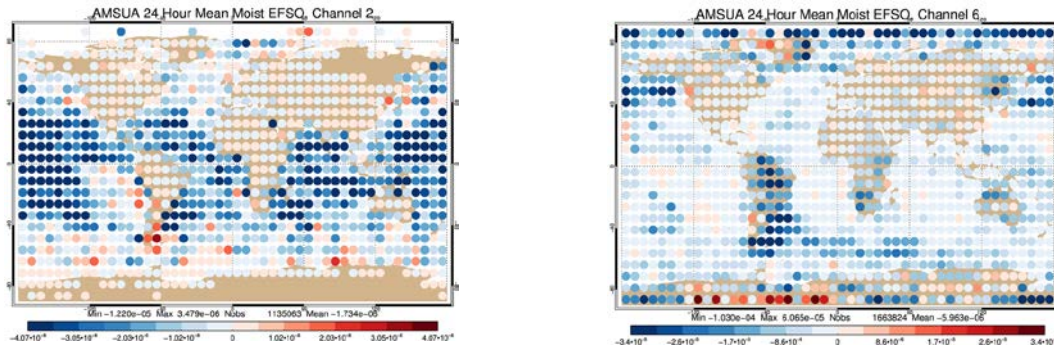


Figure 1. 7.5° by 7.5° Composite mean of 24 hour EFSO for the moist total energy norm, AMSU-A channel 2 (left panel) and AMSU-A channel 6 (right panel), the plots are for a several day sample from December 2014.

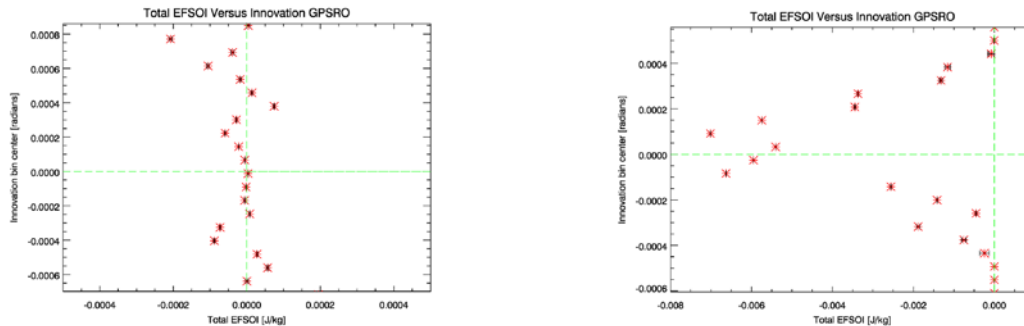


Figure 2. Total per cycle 24 hour EFSO for the moist total energy norm versus innovation bin, GPS RO Observations located below 700 hPa (left panel) and GPS RO observations located above 300 hPa (right panel), the plots are for a several day sample from January 2015.

References

- Kalnay, E., Ota, Y., Miyoshi, T. and Liu, J. 2012. A simpler formulation of forecast sensitivity to observations: application to ensemble Kalman filters. *Tellus*, 64A, 18462
- Ota, Y., Derber, J., Kalnay, E. and Miyoshi, T., 2013. Ensemble-Based Observation Impact Estimates Using the NCEP GFS. *Tellus*, 65A, 20038
- Groff, D., K. Ide, Y. Zhu and R. Mahajan, 2017, Assessment of ensemble forecast sensitivity to observation (EFSO) quantities for satellite radiances in the 4DnVar GFS. 97th AMS Annual Meeting, Washington State Convention Center, Seattle, WA.
- Whitaker, J.S., and T.M. Hamill, 2002. Ensemble data assimilation without perturbed observations. *Mon. Wea. Rev.*, **136**, 335-351
- Kleist, D. T., and K. Ide, 2015. An OSSE-based evaluation of hybrid variational- ensemble data assimilation for the NCEP GFS. Part I: 4DnVar and hybrid variants. *Mon. Wea. Rev.*, **143**, 452-470
- Todling, R., F. Diniz, L. Takacs, and M. J. Suarez 2018. Insight and evidence motivating the simplification of dual-analysis hybrid systems into single-analysis hybrid systems. 6th International Symposium on Data Assimilation, Ludwig-Maximilian University of Munich
- Ehrendorfer, M., Errico, R. M. and Raeder, K. D. 1999. Singular vector perturbation growth in a primitive equation model with moist physics. *J. Atmos. Sci.* **56**, 1627-1648

Recent updates on the usage of GNSS RO data in JMA's Operational Global Data Assimilation System

Hiromi Owada¹, Yoichi Hirahara² and Masami Moriya³

1: Office of Analysis and Applications Development, Administration Division, Observation Department, Japan Meteorological Agency

2: Numerical Prediction Division, Forecast Department, Japan Meteorological Agency

3: Satellite Application and Analysis Division, Data Processing Department, Meteorological Satellite Center, Japan Meteorological Agency

¹Corresponding author: howada@met.kishou.go.jp

Introduction

Global Navigation Satellite System (GNSS) Radio Occultation (RO) has proven to be a very important element in the global data observing system, as the measurement is an important source of atmospheric profile information for assimilation into the NWP system. The Japan Meteorological Agency (JMA) has assimilated bending angle data into its global NWP systems by introducing the Radio Occultation Processing Package (ROPP) (Culverwell et al. 2015). This paper reports on recent updates in the usage of GNSS RO data.

Updates

The relevant revisions have been evaluated and tested in the pre-processing of RO data for incorporation into the operational global assimilation system. The major updates are as follows:

- New bending angle threshold in gross error checking for the tropics
- New handling of RO quality flags (16-bit in BUFR)
- Setting of the lower altitude limit in data selection
- ROPP update from version 6 to version 8

Gross error checking is part of quality control performed before analysis based on the departure of observation and the first guess (known as the FG departure). Observations for which the absolute value of the FG departure exceeds the relevant threshold are rejected. The previous threshold was 1.5 times the observation error globally. This was stringent for the tropics because the number of bending angle observations passed through the gross error checking in the tropics was smaller than those for other areas due to the relatively large errors of tropic first guesses. The current threshold value is three times the observation error for the tropics.

Quality flagging involves 16 items of quality information added by the data processing center of each satellite. Before this update, only one item showing the quality of bending angle processing was referenced in quality control. In this update, profile quality was added as extra information to support quality control via quality flags.

In previous operation, there was no lower limit of altitude for usage. However, Metop observations exhibited a bias at altitudes below 8 km (von Engeln et al. 2009). The bias of other satellites was less severe, but was observed below 2 km. Accordingly, the lower limit of altitude for usage was set as 8 km for Metop and 2 km for other satellites.

The ROPP processing program developed by ROM SAF (the Radio Occultation Meteorology Satellite Application Facility) includes the source code for RO data assimilation. ROPP version 6 was introduced when we started to assimilate bending angle instead of refractivity in March 2014. As the new source code for

assimilation of bending angle data was added in ROPP version 8, we updated to the version 8.

Impacts on analysis

Observation system experiments for the new assimilation configuration were performed for August 2015 and January 2016. The control experiment had the same configuration as the previous operational global system, and the test experiment included the above-mentioned updates. Among the four changes, the most significant was that implemented for the bending angle threshold in gross error checking for the tropics. Figure 1 shows normalized changes in the standard deviation of the FG departure of radiosonde observation. As the reduced bending angle threshold in gross error checking increased the number of RO observations used for the tropics, the first guess profiles of radiosonde temperature were improved in the area. As a result, the first guess profiles of zonal wind were also improved.

Summary and future tasks

The usage of RO data in operational global analysis was updated on July 25 2017. After the update, the number of observation data used was increased for the upper troposphere and the stratosphere, and improved analysis of temperature and wind were confirmed there.

The above updates included the setting of a lower altitude limit below which the usage of observation data is halted. However, a November 2016 EUMETSAT update of RO data processing for Metop improved the quality of the Metop bending angle below the lower limit. In future work, data usage should be updated via careful monitoring of changes in data quality.

References

- Culverwell, I. D., H. W. Lewis, D. Offiler, C. Marquardt and C. P. Burrows, 2015: The Radio Occultation Processing Package, ROPP. *Atmos. Meas. Tech.*, **8**, 1887 – 1899.
- Von Engeln, A., S. Healy, C. Marquardt, Y. Andres and F. Sancho, 2009: Validation of operational GRAS Radio Occultation Data. *Geophys. Res. Lett.*, **36**, L17 809, DOI: 10.1029/2009GL039 968.

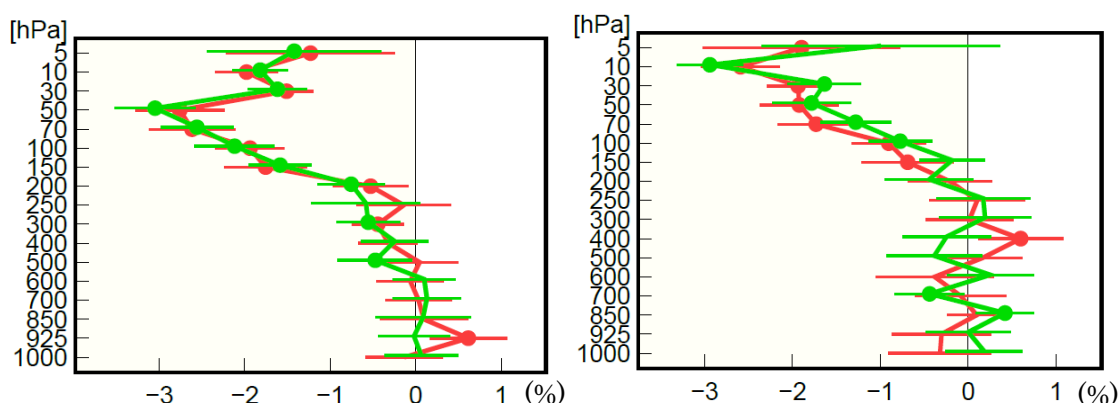


Figure 1: Normalized changes in the standard deviation of first-guess departures from radiosonde temperature (left) and zonal wind (right) in the tropics based on the experiments of August 2015 (red) and January 2016 (green). Negative values represent improvement. The horizontal axis indicates normalized standard deviation differences, error bars represent a 95% confidence interval, and dots represent statistical significance.

Data assimilation experiments of SSR mode-s downlink data using Meso-NAPEX system of JMA

Hiromu Seko¹, Ko Koizumi¹, Takayuki Yoshihara², Atsushi Senoguchi²
and Tadashi Koga²

¹Meteorological Research Institute, Tsukuba, Ibaraki, Japan

²Electronic Navigation Research Institute, Chofu, Tokyo, Japan

¹Corresponding author: hseko@mri-jma.go.jp

1. Introduction

The new air control radar system provides SSR mode-s downlink data very frequently. The horizontal wind and temperature at the positions of airplanes can be obtained from SSR mode-s downlink data that include the heading directions of airplanes, the speeds against the ground and against the airflow, the magnetic headings, and Mach numbers. Because the temporal and spatial intervals of downlink data are very short, the downlink data are expected to be useful for data assimilation of numerical weather prediction.

The data assimilation experiments on the horizontal winds of downlink data were performed by using LETKF (Local Ensemble Transform Kalman Filter; Hunt et al 2007, Miyoshi and Aranami, 2006), and showed that the rainfall forecast was improved by the assimilation of downlink data (Seko et al 2016). As the next step of this study, the quality of downlink data were investigated by the comparison with the operational mesoscale analysis data of Japan Meteorological Agency (JMA), and the data assimilation experiments of downlink data were conducted with the meso-NAPEX system (a part of JMA's 4-dimensional data assimilation system), which had been implemented to Meteorological Research Institute (MRI).

2. SSR mode-s downlink data

The downlink data observed by air control radar of the Electronic Navigation Research Institute was used in this study. It covers the Eastern and Central Japan, and its temporal interval is 10 seconds.

The horizontal wind and temperature were converted from the downlink data according to Shigetomi et al (2013). Figure 1 shows the vertical profiles of bias and RMSE between the downlink data and mesoscale analysis. The period of comparison is 30 days of September, 2015. Before the comparison, the pressures at the positions of

downlink data were obtained from their heights, because the pressures of downlink data were converted to their heights using the ICAO standard profile of atmosphere before sending to the radar.

The comparison shows that the temperature of downlink data are lower than that of mesoscale analysis data by 1 degree, and that the large difference is seen below the height of 3 km. As for the horizontal wind, there is the large difference when the airplanes were turning or ascending and descending with large speed. Then, the horizontal winds in these conditions were removed before the comparison. The bias of horizontal wind is relatively small. Considering this result, the temperature above the height of 3 km was used in the assimilation after removing the bias. The horizontal wind of whole layers were assimilated without subtracting the bias.

3. Outline of data assimilation experiments

In this study, the Meso-NAPEX system, which includes JNoVA (JMA Non-hydrostatic Model based Variational Data Assimilation System; Honda, 2008), was used. Its grid intervals of forecast and assimilation are 5 km and 15 km respectively, and its domain is the same as the operational mesoscale analysis.

The case event to which the Meso-NAPEX was applied is the intense rainfall that passed the Kanto Plain. Because the intense rainfall region and shear-lines passed the Haneda and Narita International airports, the flight operations were affected by this rainfall event. The rainfall and shear-lines were reproduced by the predictions from the initial conditions that were obtained by using the operational data only and by adding the downlink data to operational data. The impact of downlink data were indicated by the comparison with the observed ones.

4. Results of data assimilation experiments

Figure 2 shows the positions of downlink data. Many downlinks were distributed around the Haneda and Narita International airports. The results of assimilation were shown in Fig. 3. The intense rainfall was reproduced by assimilation of the operational data only (Fig. 3, left). However, the rainfall region was smaller and the rainfall was generated on the western side of the observed one. When the downlink data were assimilated, the position of rainfall region became more similar to the observed one, though the rainfall was too intense (Fig. 3, center). The positions of shear-lines were improved by the assimilation of downlink data, too. Next, the differences in the initial fields between these two experiments were investigated. The easterly flow from the eastern side of Kanto Plain became more intense when the downlink was assimilated. This result indicates that the SSR mode-s downlink data have a potential to improve forecasts of rainfalls and shear-lines, even though that the horizontal grid interval and slot interval of the assimilation are as long as 15 km and 1 hour, respectively.

Reference:

Miyoshi, T. and K. Aranami, 2006: Applying a four-dimensional local ensemble transform Kalman filter (4D-LETKF) to the JMA nonhydrostatic model (NHM). *SOLA*, **2**, 128-131.

Hunt, B. R., E. J. Kostelich and I. Szunyogh, 2007: Efficient data assimilation for spatiotemporal chaos: A local ensemble transform Kalman filter. *Physica D*, **230**, 112-126.

Honda, Y. and K. Sawada, 2008: A new 4D-Var for mesoscale analysis at the Japan Meteorological Agency. *CAS/JSC WGNE Res. Act. Atmos. Ocea. Model.*, **38**, 01.7-01.8.

Seko, H., T. Yoshihara, and A. Senoguchi, 2016: Data assimilation experiment of SSR mode-s downlink data. *CAS/JSC WGNE Res. Act. Atmos. Ocea. Model.* **46**, 1.29-1.30

Shigetomi et al., The evaluations and analyses of weather forecasts by using the SSR mode-s downlink data. *The preprints of 51st airplane symposiums, JSASS-2013-5158* (in Japanese).

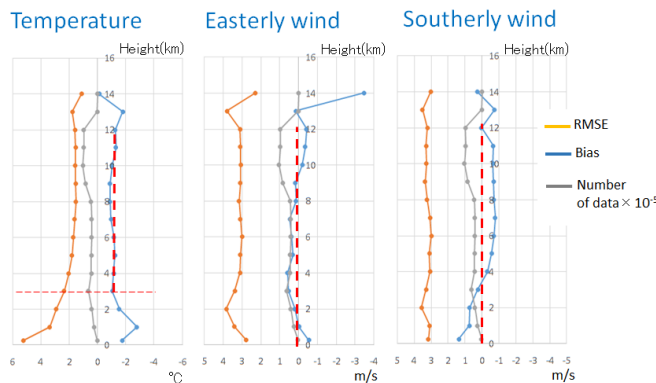


Fig.1 : Comparison between the downlink data and mesoscale analysis of JMA. Vertical profiles of the bias and RMSE of temperature, and horizontal wind.

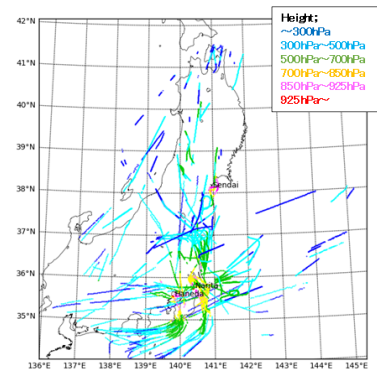


Fig.2 Positions of the assimilated downlink data. Colors indicate the height of data.

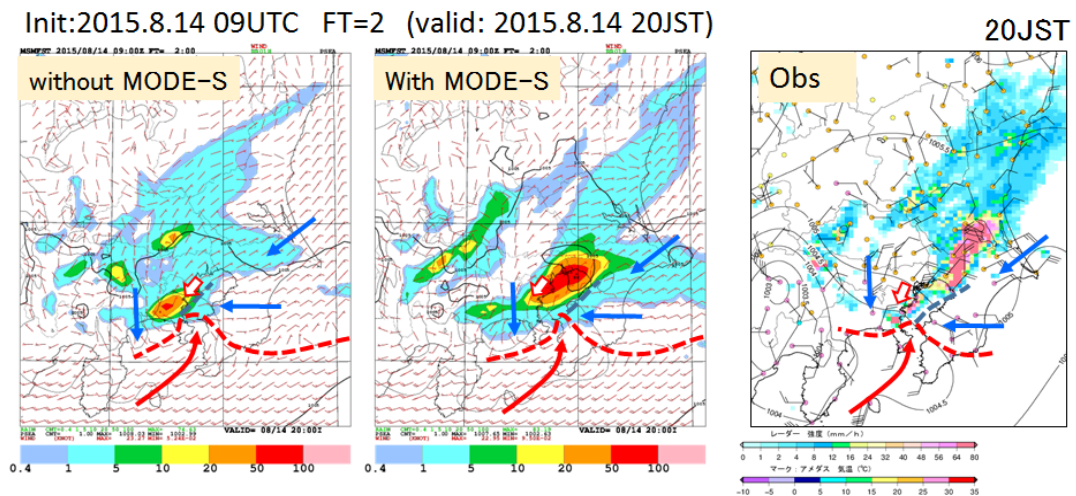


Fig. 3: Rainfall distributions predicted from the initial fields that were produced by assimilation (left) without downlink data and (center) with downlink data. (right) Observed rainfall distribution. Broken line, red and blue arrows indicate the shear-line and airflows around the rainfall region, respectively.

Operational use of Meteosat-11 Atmospheric Motion Vectors (AMVs) and Clear-Sky Radiance (CSR) Data in JMA's Global NWP System

Kazuki Shimoji, Izumi Okabe and Masahiro Kazumori
Numerical Prediction Division, Japan Meteorological Agency
E-mail: kazuki.shimoji@met.kishou.go.jp

1. Introduction

The Japan Meteorological Agency (JMA) utilizes atmospheric motion vectors (AMVs) and clear-sky radiance (CSR) data derived from Meteosats (the operational geostationary satellites of the European Organization for the Exploitation of Meteorological Satellites: EUMETSAT) to produce analysis fields in the global data assimilation (DA) system. On March 6th 2018, EUMETSAT operational satellite observing over longitude 0 deg. was switched from Meteosat-10 to Meteosat-11. Against such a background, JMA examined the data quality of AMV and CSR data from both satellites and the impacts of related data assimilation on the accuracy of numerical weather prediction (NWP).

2. Assimilation experiments

Meteosat-10 AMV data from three channels of visible (VIS, 0.635 μm), infrared (IR, 10.8 μm) and water vapor (WV, 6.25 μm) channels and CSR from the WV channel are used in JMA's global DA system. To compare the impacts of Meteosat-11 and Meteosat-10 data assimilation on the accuracy of NWP, experiments were conducted with 1) no AMVs and CSR from Meteosat-10 and -11 (BASE), 2) Meteosat-10 AMVs and CSR (CNTL), and 3) Meteosat-11 AMVs and CSR (TEST). The common quality control methods used with CNTL were applied for the TEST experiment. The experiment period was from February 7th to 26th 2018 (20 days).

3. Data quality and data assimilation impacts on the NWP system

● Meteosat-11 AMVs

Figure 1 shows histograms of the first-guess (FG) departure for the zonal wind component of AMVs. The standard deviation (STD) of the zonal (U) and meridional (V) wind components in the upper level (100 – 400 hPa) from Meteosat-11 were approximately 0.1 – 0.5 m/s for all latitude areas. These values were larger than those of Meteosat-10. Figure 2 shows histograms of FG departure (U and V components) for VIS channel lower winds. Higher STDs were observed for Meteosat-11 AMVs. However, as Meteosat-10 AMVs were

operationally used in the NWP system and quality indication (QI) with forecasts resulted in favorable judgement for Meteosat-10 winds, leading to superior statistics in terms of FG departure comparison, the qualities of the two wind values were actually comparable.

An advantage of Meteosat-11 AMVs was observed in the data counts. Those for IR/WV AMVs of Meteosat-11 were larger than those for Meteosat-10, particularly for WV AMVs (Fig. 3). The improved tracking success rate of the cloud/water vapor pattern in satellite imagery contributes to this increase. As there was no marked difference in the histograms of FG departure statistics among other Meteosat-11 AMVs and those of Meteosat-10, the data count increase was considered to stem from the higher image quality of Meteosat-11 over that of Meteosat-10.

Figure 4 shows changes in the STD of FG departure for other wind observations (radiosonde and aircraft). These changes exhibit no particular deterioration, and indeed minor improvement is observed. Thus, no particular issues were found with the use of Meteosat-11 AMVs for data assimilation.

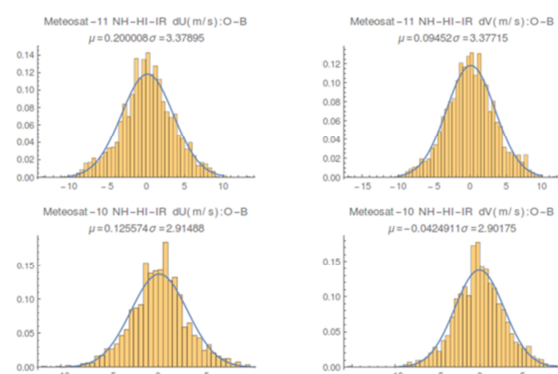


Figure 1. First-guess departure histograms of U (left) and V components (right) for IR upper-level (100 – 400 hPa) AMVs from Meteosat-11 (top) and -10 (bottom). Solid lines show normal distribution.

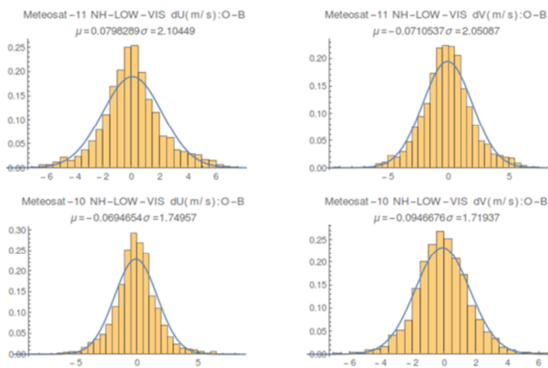


Figure 2. As per Figure 1, but for lower-level (700 – 1,000 hPa) AMVs

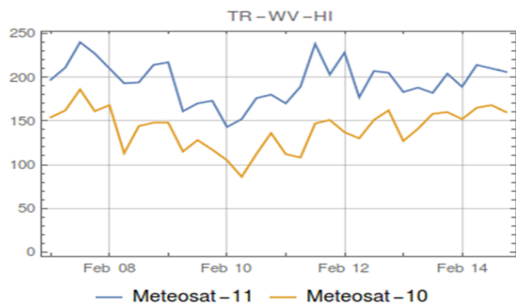


Figure 3. Time sequence plots for data counts of Meteosat-10 (yellow) and -11 (blue) active WV AMVs over the tropics

Change in standard deviation of analysis field and first guess for Radiosonde wind observation

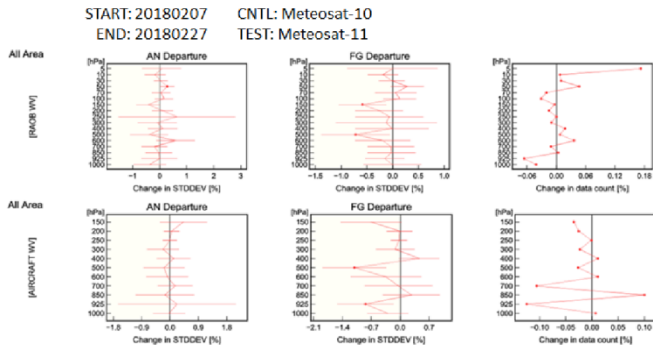


Figure 4. Changes in standard deviation of analysis fields and first guesses for wind observation (radiosonde and aircraft)

● Meteosat-11 CSR

The mean bias of the FG departure for Meteosat-11 CSR was approximately 0.16 K, and that of Meteosat-10 was -0.24 K. After variational bias correction (Ishibashi 2009), the difference in these biases was less than 0.01 K. The STD of FG departures and the data counts were very similar.

Figure 5 shows differences in the FG departure's STD for microwave humidity sounder data between CNTL and BASE (left) and those between TEST and BASE (right). Certain decreases (plotted in blue) of STD indicating improved WV fields were observed over the Meteosat observation area in both cases, indicating similar positive impacts on WV field

analysis for Meteosat-10 and -11. Consistent improvement in both sets of data was also observed with other microwave instruments (e.g., ATMS, SAPHIR and microwave imagers) as shown in Figure 6.

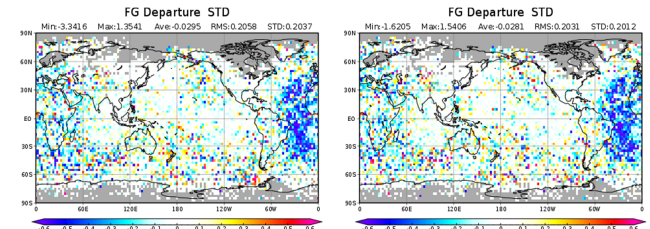


Figure 5. Differences in the first-guess departure standard deviation (STD) of microwave humidity sounding (MHS) data between CNTL and BASE (left) and between TEST and BASE (right). Blue indicates decreases (i.e., improvement) in the STD of CNTL or TEST over BASE.

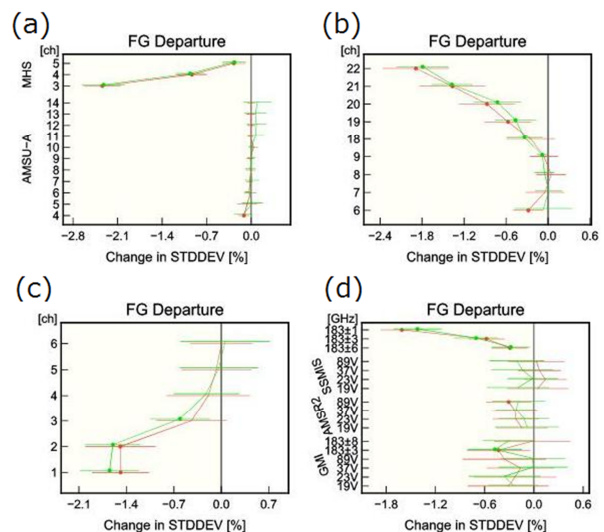


Figure 6. Normalized changes in the standard deviation of first-guess departures for (a) microwave sounding data, (b) ATMS, (c) SAPHIR and (d) microwave imager data with assimilation of Meteosat-10 (green) and Meteosat-11 (red) CSRs

4. Summary

The data qualities of AMVs and CSR from Meteosat-11 were equivalent to those of Meteosat-10, and their data assimilation impacts in NWP were similar. Based on these findings, Meteosat-11 AMV and CSR data were incorporated into JMA's operational global NWP system on March 6th 2018.

References

Ishibashi, T., 2009: Implementation of a new background error covariance matrix in the variational bias correction scheme for the JMA Global 4D-Var System. *CAS/JSC WGNE Research Activities in Atmospheric and Oceanic Modeling, Rep.*, **39**, 1 – 15.

An Algorithm for the Use of Tropical Cyclone GPS Dropsondes within Operational Numerical Weather Prediction Systems

Henry R. Winterbottom¹, Jason Sippel², Avichal Mehra³, and Vijay Tallapragada³

1 Introduction

Global positioning system (GPS) dropsondes, which are deployed during North Atlantic and Eastern Pacific ocean basins during tropical cyclone (TC) aircraft reconnaissance missions, are transmitted to the National Centers for Environmental Prediction (NCEP) and encoded using the TEMP-DROP format [1]. Currently, and for data assimilation purposes, the observation locations are specified as the GPS dropsonde launch position for all thermodynamic and kinematic variables. Although at large radii, relative to the TC center of circulation (i.e., the environment) this practice may only lead to small errors in observation positions, the errors may become very large as the circulation of the TC is encountered. For this reason NCEP rejects all wind observations within the TC vortex. In this study, we evaluate the implications upon TC track forecasts when the trajectory of the GPS dropsondes is estimated and assimilated.

2 Methodology

The reconnaissance aircraft missions considered in this study are both piloted (e.g., the NOAA P3 and the United States Air Force C-130) and unmanned (i.e., the NASA/NOAA Global Hawk). The GPS dropsondes are launched via a chute installed on the respective aircraft and a parachute is immediately deployed as the dropsonde falls. The collected observations for height, temperature, dew point-depression, wind speed, and wind direction are recorded at standard isobaric levels and encoded using the TEMP-DROP format. Also encoded are the time and location of the first wind observation (e.g., launch) and time and location of the last wind observation (e.g., surface impact).

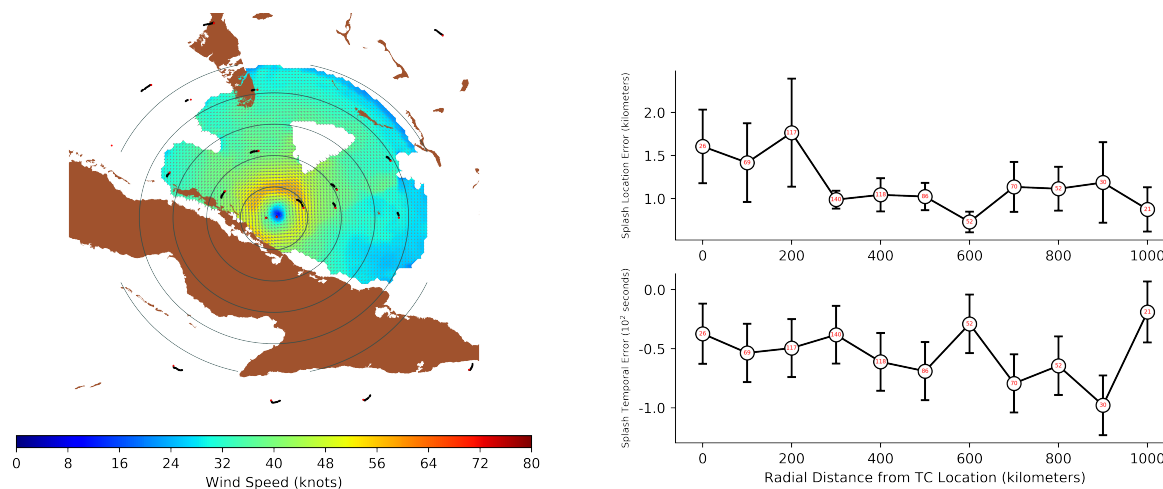


Figure 1: (left) The column integrated HRD radar winds (shaded) and wind vectors (gray arrows) valid 08 September for TC Irma (2017). The dropsonde release locations (red) and subsequent advection trajectories (black), temporally concurrent with the respective the NOAA 42 mission commencing 1710 UTC 08 September and ending 0123 UTC 09 September, are super-imposed. (right) (a) The distance and (b) temporal error error for 1147 dropsonde TEMP-DROP message encodings that contain a SPL (e.g., dropsonde impact location) message as a function of the distance from the TC center of circulation. The mean, the 95% confidence intervals, and the respective interval sample size are denoted by the black circles, error bars, and red text, respectively.

The respective TEMP-DROP observation messages are decoded into NOAA/AOML HSA formatted files

¹I. M. Systems Group (IMSG)/National Oceanic and Atmospheric Administration (NOAA)/National Centers for Environmental Prediction (NCEP)/Environmental Modeling Center (EMC); Email: Henry.Winterbottom@noaa.gov

²NOAA/Atlantic Oceanic and Meteorological Laboratory (AOML)/Hurricane Research Division (HRD)

³NOAA/National Weather Service (NWS)/NCEP/EMC

[2]. Using the launch time and location, theoretical fall-speed for the GPS dropsonde, and observed vector wind components, the advected position for the GPS dropsonde is deduced. Figure 1 illustrates the GPS dropsonde launch and predicted positions super-imposed upon the HRD composite wind analysis valid for TC Irma (2017) on 08 September. The absolute distance and time errors, as determined by computing the difference between the estimated dropsonde trajectory and surface impact information within the TEMP-DROP encoded message for all drops in Figure 1 (left), are 0.932-km and 45.4 seconds, respectively. Also provided is an analysis of the spatial and temporal errors, as a function of radial distance from the respective TC, for all GPS dropsondes containing a splash location message and collected within North Atlantic ocean basin TCs during the period 2015 - 2017.

3 Forecast Experiments

In this section, we compare results for NWP forecast experiments without GPS dropsonde drift assimilation (CNTRL) to experiments without estimation of drift or assimilation of inner-core winds (CTRL) to experiments where the drift is estimated and all winds are assimilated. The Hurricane Weather Research and Forecasting (HWRf) model provides the dynamical atmospheric predictions while the NCEP Grid-point Statistical Interpolation (GSI) system enables the assimilation of all atmospheric observations.

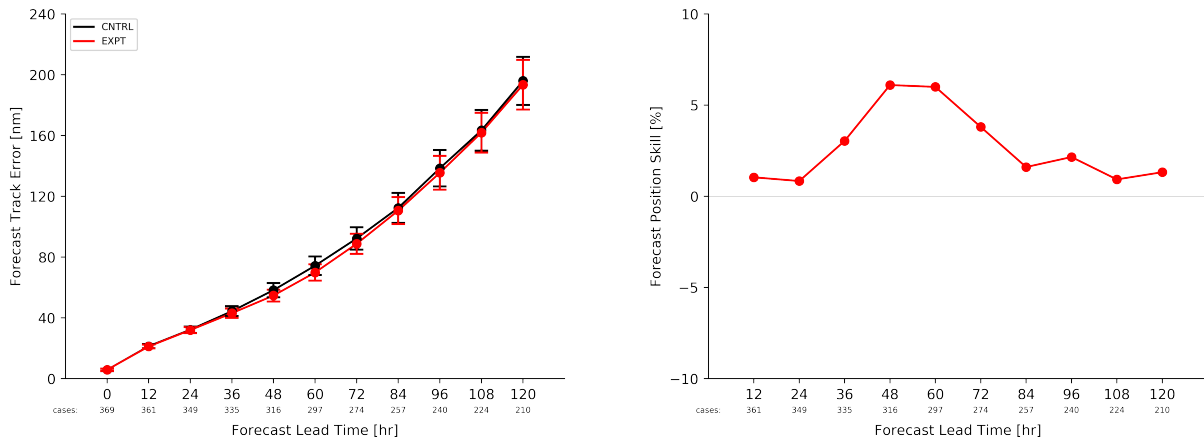


Figure 2: (left) The TC track forecast error for CNTRL (black) and EXPT (red) compared to observations and (right) the TC track forecast skill for EXPT (red) compared to CNTRL.

Figure 2 (left) illustrates the TC track forecast error (compared to observations) for EXPT and CNTRL and (right) the TC track forecast skill for EXPT when compared to the baseline experiment (CNTRL). Overall, the TC track forecast error is reduced for EXPT, in particular at medium range forecast lead times. This is further illustrated when assessing the TC track forecast skill at medium range lead-times where the improvement is on the order of nearly 7%.

4 Ongoing Research and Future Applications

The 2018 NCEP operational HWRf forecasting system will include dropsonde drift assimilation when reconnaissance observations are available.

References

- [1] S. D. Aberson, K. J. Sellwood, and P. A. Leighton, “Calculating dropwindsonde location and time from temp-drop messages for accurate assimilation and analysis.,” *Journal of Atmospheric and Oceanic Technology*, vol. 34, pp. 1673–1678, 2017.
- [2] J. L. Franklin, S. E. Feuer, J. Kaplan, and S. D. Aberson, “Tropical cyclone motion and surrounding flow relationships: Searching for beta-gyres in omega dropwindsonde datasets.,” *Monthly Weather Review*, vol. 124, pp. 64–84, 1996.

Preliminary assessment and assimilation of Himawari-8 Rapid Scan Atmospheric Motion Vector data for typhoons

Koji Yamashita

Numerical Prediction Division, Japan Meteorological Agency
Current position: Meteorological Satellite Center, Japan Meteorological Agency
e-mail: kobo.yamashita@met.kishou.go.jp

1. Introduction

The Meteorological Satellite Center of the Japan Meteorological Agency (JMA/MS-C) has produced operational Himawari-8 Atmospheric Motion Vectors (AMVs) since July 7th 2015 (Bessho et al. 2016). The data are created using three sequential satellite images with temporal intervals of 10 minutes on an hourly basis. To support the provision of wind data relating to meso-scale phenomena and typhoons, JMA/MS-C started operational generation of rapid-scan AMVs (RS-AMVs) based on Himawari-8 rapid-scan imagery in July 2017 for JMA's internal assessment. These RS-AMVs are produced every 2.5 minutes for a domain covering Japan and an additional small domain covering a typhoon presents over the western North Pacific (Fig. 1 (a)). RS-AMVs for typhoons are expected to clarify the fine structure of typhoon wind fields better than operational AMVs (Fig. 1). Accordingly, the assimilation of RS-AMV data is expected to improve typhoon analysis and forecasting skill.

2. Quality of RS-AMVs for five typhoons

RS-AMVs retrieved by JMA/MS-C for five typhoons (Soudelor, Goni and Dujan in 2015, and Nepartak and Megi in 2016) were used for data quality assessment. The data were validated against dropsonde (DOTSTAR; Wu et al. 2005) and sonde observations, and against first-guess (FG) wind data from JMA's global model. Validation was performed for each of the five cases.

The results showed that RS-AMV wind speeds exhibited a negative bias against sonde observations, especially over mid- and lower-levels, and occasionally against the FG (Table 1). This may be attributable to the significant difference in the vertical levels of wind speed shear between sonde and RS-AMV data (Fig. 2). Root mean square vector differences (RMSVDs) of RS-AMVs were larger than those of operational AMVs (RMSVD: 5 – 6 m/s) against sonde observations. Comparison of the five cases indicates that wind data for Typhoon Nepartak were more accurate than in the other cases (Table 1 and Fig. 2).

3. Typhoon RS-AMV observing system experiments (OSEs) with JMA's global NWP system

OSEs were performed for Typhoon Nepartak (for which data quality was the best of the five typhoons examined; see Section 2) with JMA's global NWP system for the period from July 1 to July 20 2016. Here, the term CNTL refers to an experiment involving assimilation of Himawari-8 AMVs processed using 1) the 100-km super-observation technique (100kmSPOB; Yamashita 2014) for the area over Japan and surrounding areas, and 2) 200-km thinning over other regions. TEST refers to an experiment involving assimilation of Himawari-8 RS-AMVs for typhoons processed with 100kmSPOB, in addition to the AMVs assimilated in CNTL. The Himawari-8 typhoon RS-AMVs were processed using 100kmSPOB to promote effective use of data from the area around the typhoon center. A larger body of AMV data was assimilated for the area around the typhoon center in TEST than in CNTL (Fig. 3). The typhoon track forecasts observed the experiments were verified against typhoon best track (BST) data provided by the Regional Specialized Meteorological Center (RSMC) Tokyo – Typhoon Center. Quality control for the wind data in both experiments was as per that of the operational NWP system. The OSE results showed neutral impacts on typhoon track forecasts. The typhoon intensity forecasts in TEST were weaker than in CNTL (Fig. 4). However, as shown in Fig. 5, forecast errors were reduced along the typhoon track areas at 500-hPa geopotential height.

More case studies are needed to clarify impacts from assimilation of RS-AMVs for typhoons.

4. Conclusions

The quality of Himawari-8 RS-AMVs for typhoons in five cases was evaluated using DOTSTAR dropsonde observation data and FG wind data from JMA's global model. The results indicated that RS-AMV wind speeds exhibited a negative bias against both data types. Meanwhile, assimilation experiments involving RS-AMV data demonstrated partially improved typhoon structures in JMA's

global NWP system. Further investigation is needed to elucidate the mechanism behind differences in typhoon structure forecasts with RS-AMV data assimilation.

Acknowledgments

JMA is grateful to DOTSTAR project staff for their provision of the data used in this study.

References

Bessho, K., K. Date, M. Hayashi, A. Ikeda, T. Imai, H. Inoue, Y. Kumagai, T. Miyakawa, H. Murata, T. Ohno, A. Okuyama, R. Oyama, Y. Sasaki, Y. Shimazu, K. Shimoji, Y. Sumida, M. Suzuki, H. Taniguchi, H. Tsuchiyama, D. Uesawa, H. Yokota and R. Yoshida, 2016: An introduction to Himawari-8/9 – Japan's new-generation geostationary meteorological satellites. *J. Meteor. Soc. Japan*, 94.

Yamashita, K., 2014: Observing system experiments of MTSAT-1R rapid scan AMVs using JMA's operational NWP system from 2011 to 2013. *Proc. 12th Int. Winds Workshop*, Copenhagen, Denmark, EUMETSAT.

Wu, C.-C., P.-H. Lin, S. D. Aberson, T.-C. Yeh, W.-P. Huang, J.-S. Hong, G.-C. Lu, K.-C. Hsu, I.-I. Lin, K.-H. Chou, P.-L. Lin and C.-H. Liu, 2005: Dropwindsonde observations for typhoon surveillance near the Taiwan Region (DOTSTAR): an overview. *Bull. Amer. Meteor. Soc.*, 86, 787 – 790.

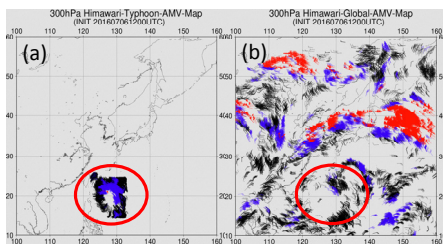


Figure 1: Himawari-8 AMV data coverage (a: RS-AMVs for a typhoon (approx. 4-km res.); b: operational AMVs (approx. 50-km res.) at 12 UTC on July 6 2016 for analysis of Typhoon Nepartak (AMVs: red: ≥ 50 kt; blue: ≥ 30 kt; black: < 30 kt)

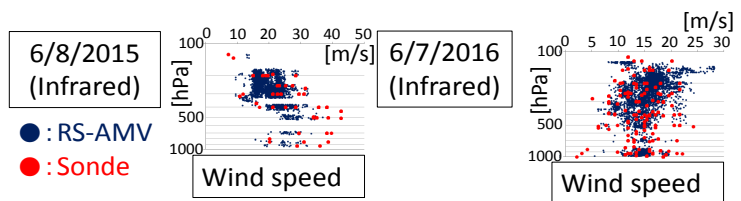


Figure 2: Wind speed vertical distributions of RS-AMVs for typhoons and wind sonde observation at 1104 UTC for August 6 2015 (Soudelor) and July 6 2016 (Nepartak)

Table 1. Results of typhoon RS-AMV validation against sonde winds and wind forecasts in five case studies. Bxx: Himawari-8 band number; ME: mean error of wind speed [m/s]; RMSVD: root mean square wind vector difference [m/s]; HL: 10 – 400 [hPa], ML: 400 – 700 [hPa], LL: 700 – 1,000 [hPa].

YYYYMMDDHH (Typhoon name)		2015080612 (Soudelor)		2015082000 (Goni)		2015092700 (Dujuan)		2016070612 (Nepartak)		2016092600 (Megi)	
Vs. Forecast		ME	RMSVD	ME	RMSVD	ME	RMSVD	ME	RMSVD	ME	RMSVD
B13 AMV (Infrared)	HL	0.33	6.69	0.04	6.16	-0.01	6.00	0.29	3.80	-0.46	5.74
	ML	-2.42	6.83	0.12	6.51	-1.13	4.44	0.27	2.99	-0.23	3.47
	LL	-1.10	4.83	0.00	3.49	0.38	4.02	-1.14	3.65	-0.18	3.21
Vs. Sonde		ME	RMSVD	ME	RMSVD	ME	RMSVD	ME	RMSVD	ME	RMSVD
ALL AMV (B03-B16)	HL	-5.03	11.28	-6.77	10.98	-1.49	6.89	0.63	5.53	-1.82	7.68
	ML	-4.17	10.14	-8.65	16.12	-2.55	7.11	-0.50	6.03	-4.46	7.86
	LL	-2.37	7.45	2.72	9.05	-1.36	6.70	0.58	5.01	0.14	6.58

Figure 3: AMV data coverage after QC around Typhoon Nepartak in CNTL (left) and TEST (right) for 06 UTC on July 4 2016

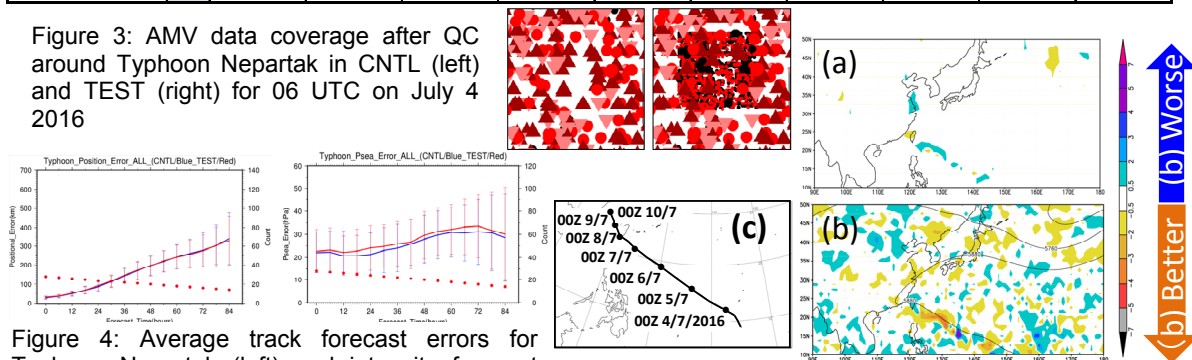


Figure 4: Average track forecast errors for Typhoon Nepartak (left) and intensity forecast errors (sea level pressure; right). The red line shows TEST values, the blue line shows CNTL values, and red dots show sample data numbers. Error bars represent a 95% confidence interval.

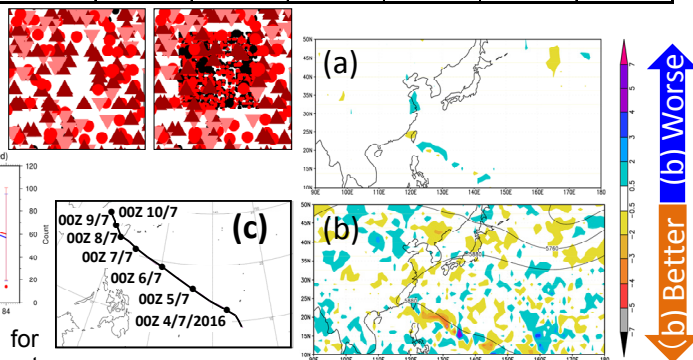


Figure 5: Mean error differences (a) and normalized root mean square error differences (b) between TEST and CNTL for 12-hour forecast lead times at 500-hPa geopotential height. (c) Typhoon Nepartak BST track.